

OBLIQUE IMPACT MODELING OF FUZES

GEORGE A. GAZONAS[†], STEVEN B. SEGLETES, VINCENT M. BOYLE
 and STEVEN R. STEGALL

U.S. Army Research Laboratory, Weapons Technology Directorate, Aberdeen Proving Ground,
 MD, 21005-5066, U.S.A

(Received 25 November 1994; in revised form 3 July 1995)

Summary—This paper presents the results of a combined experimental, numerical, and analytical investigation of a low-speed (198 m/s) oblique impact of a cylindrical steel projectile into an aluminum–brass composite fuze simulant. The numerical simulations were performed prior to the experiments using the Lagrangian hydrocode EPIC92. The results indicate that projectile hardness and impact point strongly influence the mechanism by which the fuze deforms. An experiment was then conducted in order to evaluate the predictive capabilities of the hydrocode. The experimental results generally corroborate the hydrocode results during the initial stages of the impact but depart significantly at later stages of the penetration. Possible causes for the observed differences between the experiment and the simulation include, (i) the absence of a global fracture modeling capability in the hydrocode, and (ii) boundary condition differences between experiment and simulation. The hydrocode predicts that 91% of the projectile kinetic energy is converted into target plastic work. This result compares well with predictions based upon an analytical model of an elastic–plastic beam bent by an end load.

NOTATION

A, B, C, n, m	Johnson–Cook constitutive model constants
D	EPIC damage parameter
D_1, D_2, \dots, D_5	Johnson–Cook fracture model constants
dA	beam area increment
D_{ijkl}	elastic modulus tensor
E	Young's modulus
e	limit of elastic behavior (Fig. 12b)
h, h_a, h_b	beam diameter, tapered beam diameter at tip and built-in end
I	beam moment of inertia
L	beam length
M, M_y, M_p	beam moment, yield moment, plastic moment
P, P_y	load, load at initial yield (Fig. 12a)
T^*	homologous temperature
U, U^*, U_{Tot}	dimensionless strain energy, complementary energy, total energy
v, v_{max}	elastic beam deflection, maximum elastic tip deflection
x, x_1	beam axial coordinate, limit of elastic behavior
y	beam coordinate (Fig. 12b)
δ, δ_y	beam tip deflection, tip deflection at initial yield
$d\sigma_{kl}, d\epsilon_{ij}, d\epsilon_{ij}^p$	incremental stress, strain and plastic strain tensors
$\dot{\epsilon}, \dot{\epsilon}_0, \dot{\epsilon}^*$	strain rate, normalization strain rate, dimensionless plastic strain rate
$\epsilon^f, \epsilon^p, \Delta\epsilon^p$	fracture strain, equivalent plastic strain, incremental equivalent plastic strain
κ, κ_y	beam curvature, beam curvature at initial yield
$\sigma, \sigma_y, \bar{\sigma}, \sigma^*$	beam stress, maximum yield stress, equivalent stress, pressure–stress ratio
$\sigma_m, \sigma_{max}, \sigma_b, \rho'_{ij}$	mean normal stress, max. beam stress, max. bending stress, deviatoric stress

1. INTRODUCTION

There are a number of munition-related problems of interest to the defense community in which the presence of energetic materials is integral. One such area of investigation is that of explosive ordnance disposal (EOD) render-safe procedures, in which a potentially armed and thus dangerous fuze is disabled *in situ*, in order to render it safe for subsequent handling and

[†] Author to whom correspondence should be addressed.

removal. One class of render-safe methods might be termed “mechanical”, in that it relies on a measured use of mechanical force to sever or disrupt the explosive initiation train within the fuze.

One such mechanical technique to render a fuze safe is to impact it with a hardened projectile at an oblique angle, for example, perpendicular to the fuze’s axis of symmetry. With the proper selection of impact location and speed, the mechanical damage induced by the impact can be made sufficiently brisant to isolate the high explosive primer material from subsequent stages of the high explosive train. However, the impact should not shock the fuze to an extent which causes the explosive material to initiate. The EOD community currently employs this mechanical method in certain render-safe procedures.

The physical process of rendering a fuze safe *in situ* can be quite hazardous. In addition, certain types of foreign-made ordnance are of limited supply, and not available for parametric testing. For these reasons, it is recognized that numerical simulation may assist in the development of render-safe procedures. To this end, this paper reports an investigation into the suitability of employing the EPIC92 hydrocode in the modeling of an oblique fuze impact, a mechanical render-safe procedure. The corresponding experiment was performed after the simulation work was completed, to provide a direct comparison for the simulation results. Another advantage of conducting the numerical analyses prior to the impact experiment is in determining the best time to radiograph the fuze. Upon introducing the specifics of the idealized problem to be studied, the problem geometry, constitutive properties and boundary conditions of the problem are described. The results of finite element numerical simulations and experiment are presented and compared. Finally, an elastic–plastic analytical solution is developed, which sheds insight into fuze render-safe mechanics, and is compared with the hydrocode results.

2. PROBLEM DESCRIPTION

The current work focuses on investigating the “structural” damage (i.e. the mechanical response) imparted to an inert fuze simulant as a result of an oblique impact, rather than establishing the impact conditions that are necessary to render-safe an actual fuze device.

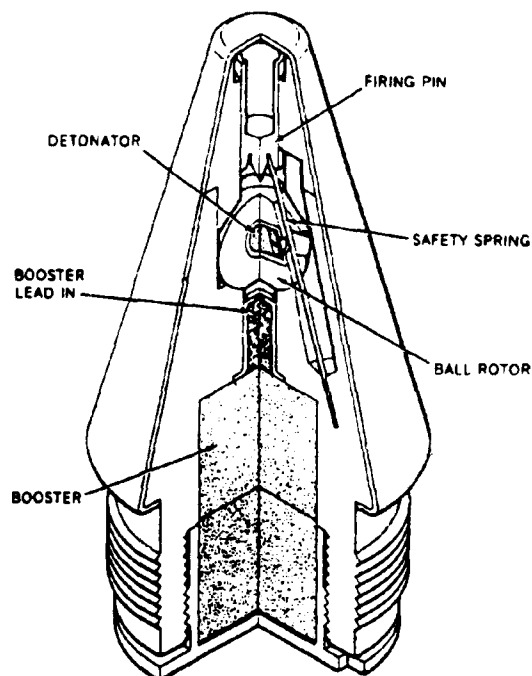


Fig. 1. Cutaway view of a typical fuze, illustrating internal components.

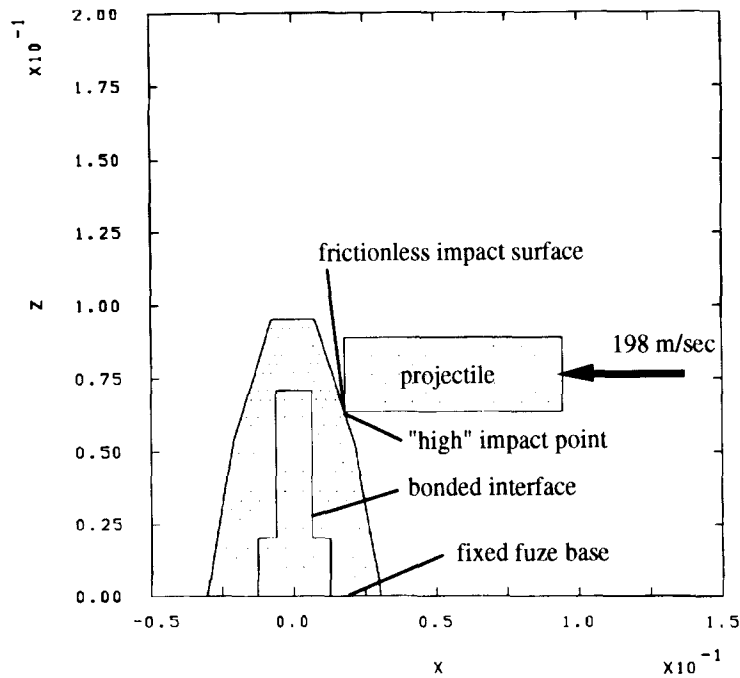


Fig. 2. Fuze and projectile boundary conditions (dimensions in meters).

Only after a proper understanding of the mechanical response is obtained may future work address the complete fuze render-safe problem by replacing the inert components of the fuze simulant with an explosive material. Hereafter, the fuze simulant will simply be referred to as the fuze.

A typical fuze geometry consists of a right-circular cone that threads into the ordnance at its base (Fig. 1). The cutaway view also illustrates some of the important internal fuze components such as the firing pin, detonator and booster. Although these components are critical for proper operation of the fuze under normal impact conditions, replacing the "fine" internal structure of the fuze with a homogeneous core material will simplify the oblique impact problem.

The fuze selected for analysis comprises an axially symmetric 6061-T6 aluminum sheath surrounding a softer brass core. The aluminum sheath is 2.40 in. (61.0 mm) in diameter at the base, and tapers bilinearly from base to apex. The fuze height is 3.72 in. (94.5 mm). The projectile consists of a solid, hard steel, right circular cylinder, 1 in. (25.4 mm) in diameter and 3 in. (76.2 mm) long, with a mass of 300 g. It is designed to strike the fuze normal to its axis of symmetry during standard render-safe procedures. The initial configuration as modeled, is shown in Fig. 2, including a typical hit location and impact velocity. The specific engagement configurations for the three numerical simulations and single experiment were provided by Patel and Gold [1] (see Sections 3.2 and 5).

It should be pointed out that in an actual oblique impact render-safe procedure, the barrel of the gun which launches the projectile is kept in close proximity to the target fuze. This actual configuration has the effect of providing lateral confinement on the projectile. However, both experiment and simulations are performed with a free-flying projectile, because a more proximate gun position might obscure the photographic coverage with propellant combustion products. This lack of lateral confinement has two effects: it permits projectile rotation after impact, and it reduces the accuracy of the aim in the experiment.

3. NUMERICAL APPROACH

A number of hydrocodes (for example CTH [2], SPH [3], CALE [4], EPIC [5–7], MESA [8], HULL [9], and DYNA [10]) are available to numerically simulate the render-safe

impact event in question. The term “hydrocode” describes that class of continuum mechanics based numerical codes capable of solving wave propagation problems. This investigation uses the Lagrangian-based explicit EPIC92 (*Elastic–Plastic Impact Calculations*) hydrocode [5–7], because of: (i) previous impact modeling experience with EPIC92 and other similar Lagrangian-based hydrocodes [11], and (ii) EPIC’s capabilities for modeling ignition and detonation phenomena in explosive materials [6, 7, 12]. This explosive modeling capability will permit future efforts to model a more realistic fuze configuration while at the same time retain compatibility with the current series of simulations.

Since the three-dimensional dynamic equations of motion for the oblique fuze impact problem are intractable to solve in closed form, finite element methods are employed to obtain approximate solutions to the problem. A complete description of any boundary value problem in continuum mechanics involves specifying the geometry, boundary conditions, constitutive equations and failure or instability criterion. The finite element solution for the unknown field variables (typically displacements) over the domain of interest proceeds by using the method of weighted residuals or through the development of a variational principle for the problem (see Zienkiewicz [13] for a good review of finite element methods). As described in Zienkiewicz [13], a global stiffness matrix is assembled at each time step to obtain a finite element solution. Alternatively, the equations of motion are directly integrated in EPIC92, thus circumventing the need for the formation of a stiffness matrix [5].

3.1. *Geometry*

A typical fuze geometry consists of a right-circular cone that threads into the projectile (Fig. 1). The cutaway view also illustrates the important internal fuze components such as the firing pin, detonator, and booster. Although these complex components are necessary for operation of the fuze under normal impact conditions, we replace them with a homogeneous material to simplify the analysis. Thus, the fuze model consists of an axially symmetric outerbody that encases an inner homogeneous core as shown in Fig. 2. The base of the fuze is 2.40 in. (61 mm) in diameter and the fuze height is 3.72 in. (94.5 mm) (Fig. 2). The projectile consists of a solid right-circular cylinder, 1.0 in. (25.4 mm) in diameter and 3.0 in. (76.2 mm) long, and impacts the fuze normal to its axis of symmetry during EOD render-safe procedures.

3.2. *Boundary conditions*

The boundary conditions are usually of mixed-type and are given in terms of displacements, forces, or their first time-derivatives. The fuze is assumed to be rigidly fixed at the base so that all x -, y -, and z -displacements vanish on the base surface (Fig. 2). We believe this assumption will not severely affect the results because the base of the actual fuze is tightly screwed into the ordnance (Fig. 1). Since the core material is press-fitted into the fuze outerbody, in the simulation we assume that the homogeneous brass core material is bonded to the fuze outerbody (Fig. 2). The projectile impact velocity is 198 m/s and numerical solutions are sought for two impact points along the vertical fuze axis (Fig. 2). One impact point is 1.25 in. (31.75 mm) below the top of the fuze and the other impact point is 0.50 in. (12.7 mm) above the base of the fuze; the bottom edge of the projectile impacts the fuze at these positions.

Finally, we assume that the contact surface between the projectile and the fuze is frictionless. It is difficult to estimate the severity of this assumption because of the lack of dynamic friction data for these materials. However, friction effects dominate the interactions of bodies in very low-speed or quasistatic contact problems. Thus, in the late stages of the impact event, as the projectile decelerates, friction will play a more important role in the interactions. A three-dimensional slide line algorithm permits the Lagrangian-based hydrocode to accommodate the severe distortions encountered in impact problems. This algorithm typically involves defining a master and slave surface, so as to prevent element interpenetration. A master surface and slave surface exist for both the projectile and the fuze in this analysis.

3.3. Constitutive equations

The fuze outerbody material consists of 6061-T6 aluminum (EPIC92 material model 23) that encases an inner core of gun-cartridge brass (EPIC92 material model 2) (Fig. 2). The projectile material consists of 4340 (EPIC92 material model 9). The initial simulation results reveal that the projectile deforms more than that anticipated (Patel and Gold [1]). In subsequent analyses, we use a harder steel projectile, with a hardness of Rockwell C (R_c) R_c57 . The properties of this material are based upon a modification of an $R_c 50$, S-7 tool steel (EPIC92 material model 10) with a modified initial yield stress; the magnitude of the modified yield stress is based upon an empirical correlation that exists between Rockwell hardness and yield strength in various metals (see Oberg *et al.* [14]). The fuze deformation mechanisms observed for projectiles with these hardness values (R_c30 and R_c57) are very different, and therefore will be discussed and compared in more detail in Section 4.

The Johnson–Cook viscoplastic constitutive model is used in the analysis together with a von Mises initial yield condition [15, 6, 7]. An isotropic hardening rule governs subsequent yield surface behavior. The equivalent uniaxial stress, $\bar{\sigma}$, is defined as

$$\bar{\sigma} = \sqrt{\frac{3}{2} \sigma'_{ij} \sigma'_{ij}}, \quad (1)$$

in which σ'_{ij} is the deviatoric stress tensor. The Johnson–Cook model incorporates strain, strain rate, and thermal softening effects where the corresponding parameters functionally appear in multiplicative form as,

$$\bar{\sigma} = [A + B\bar{\epsilon}^n][1 + C \ln \dot{\epsilon}^*][1 - T^{*m}], \quad (2)$$

in which $\bar{\epsilon}^p$ is the equivalent time-dependent uniaxial plastic strain defined by,

$$\bar{\epsilon}^p(t) = \int_0^{\bar{\epsilon}^p(t)} d\bar{\epsilon}^p = \int_0^{\bar{\epsilon}^p(t)} \sqrt{\frac{2}{3} d\epsilon^p_{ij} d\epsilon^p_{ij}}, \quad (3)$$

and $d\epsilon^p_{ij} \sim d\epsilon_{ij} - D_{ijkl} d\sigma_{kl}$, D_{ijkl} is the fourth rank elastic modulus tensor. $\dot{\epsilon}^* = \dot{\epsilon}/\dot{\epsilon}_0$ is the dimensionless plastic strain rate for $\dot{\epsilon}_0 = 1 \text{ s}^{-1}$, and T^* is the homologous temperature. The material constants A, B, C, n , and m are determinable from material tests conducted at different strains, strain rates, and temperatures [6–7]. The equivalent adiabatic flow stress vs equivalent plastic strain plots at strain rates of 1, 100 and $10,000 \text{ s}^{-1}$ are derived from the EPIC92 material library constants (Fig. 3). All of the materials (except for brass) exhibit work-softening behavior which is a result of adiabatic thermal softening of dynamically strained material, rather than strength loss due to microcracking or other damage mechanisms.

3.4. Damage and erosion criteria

The damage criterion in EPIC92 is assumed to be a scalar function of the incremental (cumulative) equivalent plastic strain, $\Delta\bar{\epsilon}^p$, normalized with respect to the strain at fracture, ϵ^f . [6, 7]:

$$D = \frac{\sum \Delta\bar{\epsilon}^p}{\epsilon^f}; \quad (4)$$

where ϵ^f takes on a similar multiplicative form to that of Eqn (2),

$$\epsilon^f = [D_1 + D_2 e^{D_3 \sigma^*}][1 + D_4 \ln \dot{\epsilon}^*][1 + D_5 T^*], \quad (5)$$

in which $\sigma^* = \sigma_m/\bar{\sigma}$ is the pressure–stress ratio, σ_m is the pressure (mean stress), and D_1 through D_5 are independent material constants determined from fracture experiments. If $D \geq 1$ in Eqn (4) in a given finite element, the element can only sustain additional hydrostatic compressive stress but not shear or tensile stresses. Unlike other finite element codes which can model the propagation of discrete fracture surfaces in the finite element mesh [16], EPIC92 cannot simulate such behavior. EPIC92 does have the capability of handling severe distortions encountered in penetration problems, however, through an element erosion algorithm which eliminates element volume, but retains element mass, when a critical value of $\bar{\epsilon}^p$ is reached. In the current analysis, we consider that element volume erodes when $\bar{\epsilon}^p = 1.5$.

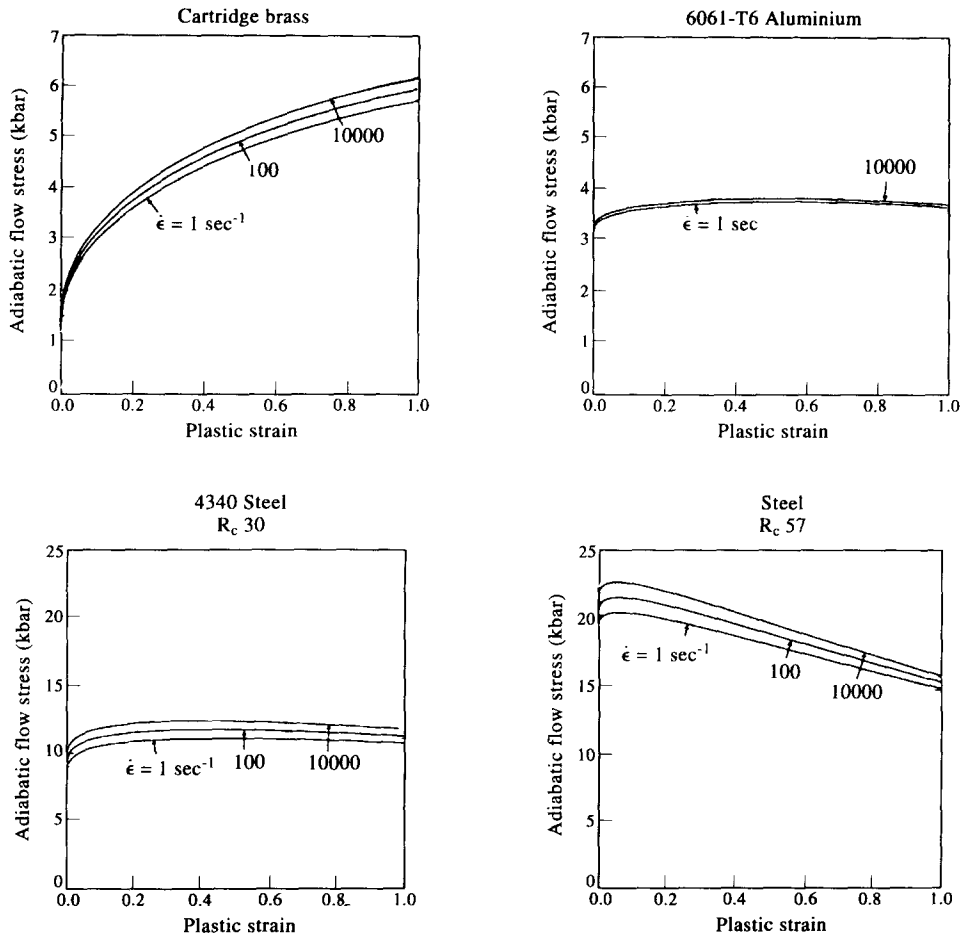


Fig. 3. Adiabatic flow stress vs equivalent plastic strain curves as a function of strain rate for gun cartridge brass, 6061-T6 aluminum and 4340 and modified S-7 tool steels.

- 544 symmetric brick finite elements
- 24 tetrahedral elements per brick
- 13,056 total tetrahedral elements
- 4 constant strain triangles per tetrahedron
- 52,224 CST's

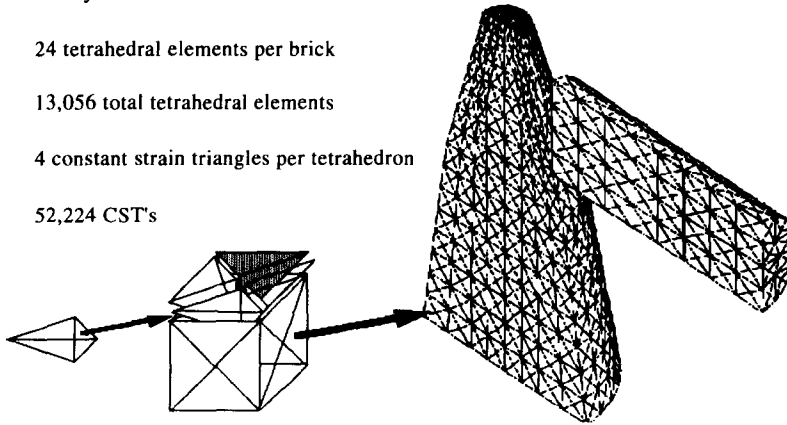


Fig. 4. Finite element mesh used in numerical simulations.

4. NUMERICAL RESULTS

The three-dimensional finite element mesh used to model the fuze consists of 544 symmetric brick finite elements; each brick element contains 24 tetrahedral elements that are formed by linking four constant strain triangles (CST's) (Fig. 4). There are a total of 13,056 tetrahedral elements. The low-order displacement field within each CST element necessitates

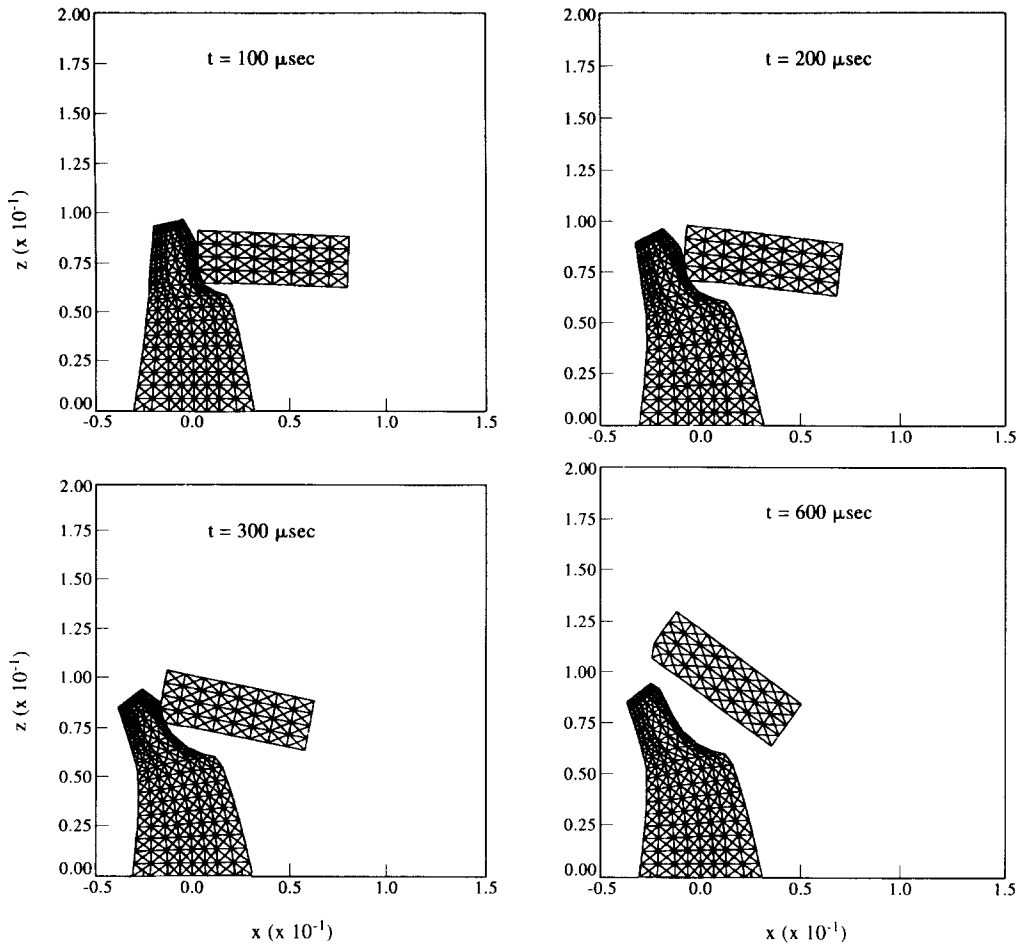


Fig. 5. Event 1. "Soft" high-impact EPIC92 hydrocode results.

the use of more elements in regions of high deformation gradient. One advantage of conducting the numerical analyses prior to the impact experiment is in determining the best time to radiograph the fuze. The results of the three-dimensional EPIC92 numerical simulations appear in Figs 5–7. Figure 5 illustrates the "soft" projectile (R_c30) high-impact point results. Figures 6 and 7 illustrate the "hard" projectile (R_c57), high-impact and low-impact results, respectively.

4.1. Event 1. "Soft" projectile, high-impact point

The "soft" projectile impacts the fuze ogive normal to the fuze axis of symmetry at a position located 1.25 in. (31.75 mm) below the top (measured along the fuze axis) of the fuze. The projectile plastically deforms and rotates clockwise as it progressively slips towards the fuze apex (projectile rotation sense is relative to that shown in Figs 5–7). The projectile's slipping motion scours a continuous groove, of elliptical form, into the fuze's surface. However, the groove is not so deep so as to expose the inner brass core of the composite fuze. After approximately 420 μ s of continuous contact, the projectile slips off the end of the fuze and continues rotating clockwise. After 1200 μ s, the rear edge of the projectile rotates sufficiently to hit the fuze in a secondary impact event; this impact causes only minor additional fuze deformation. Because the projectile sustains large permanent deformations in our simulations, while Patel and Gold [1] have observed that the projectile is relatively undeformed after impact, subsequent simulations use a harder steel projectile on the order of Rockwell C57. The "hard" projectile material properties are essentially that of an S-7 tool steel (see Section 3.3. *Constitutive equations*).

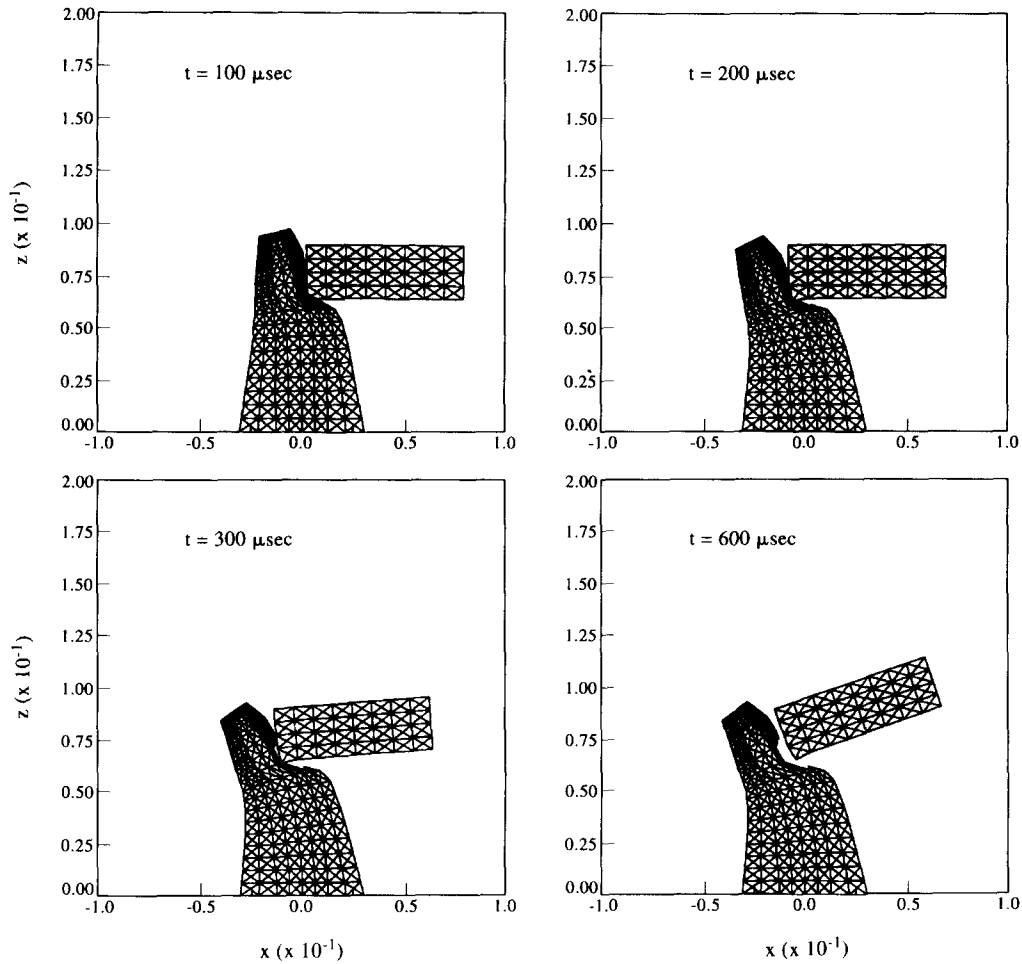


Fig. 6. Event 2. “Hard” high-impact EPIC92 hydrocode results.

4.2. Event 2. “Hard” projectile, high-impact point

Under identical impact conditions, and in contrast to the “soft” projectile impact, the “hard” projectile impact is relatively slip-inhibited and results in a greater penetration depth into the fuze than with the “soft” projectile. The “hard” projectile slips a negligible distance in the vertical direction, however, and rotates counterclockwise rather than clockwise, which can be seen by comparing Figs 5 and 6 at an elapsed time of $200 \mu\text{s}$. As in the “soft” impact event, the “hard” impact does not expose the brass core of the composite fuze. However, the “hard” projectile causes more deformation in the fuze than the “soft” projectile; a comparison of deformed meshes at $300 \mu\text{s}$ in Figs 5 and 6 shows a greater degree of bending in the fuze impacted by the “hard” projectile. Hence, it appears that a “soft” projectile impact will cause less fuze damage due to slip and permanent projectile deformation; the “hard” projectile causes more bending in the fuze and the projectile sustains less permanent deformation. The contact duration for the “hard” projectile high-impact is about $500 \mu\text{s}$, which exceeds the durations of the other two impact events.

Equivalent plastic strain, $\bar{\epsilon}^p$, contours aid in visualizing the permanent deformation history of the fuze (Fig. 8). Equivalent plastic strain is a scalar representation of the tensorial strain state. The $\bar{\epsilon}^p = 0.20$ contours develop asymmetrically beneath the edge of the projectile after $20 \mu\text{s}$. Plastic strain then spreads through the aluminum outerbody and reaches the brass core at $40 \mu\text{s}$ (Fig. 8a). With increased projectile penetration and fuze bending, plastic deformation also appears on the back side of the fuze, and achieves $\bar{\epsilon}^p = 0.20$ at $120 \mu\text{s}$. The plastic zones eventually merge to form a plastic “hinge” through the cross-section of the fuze.

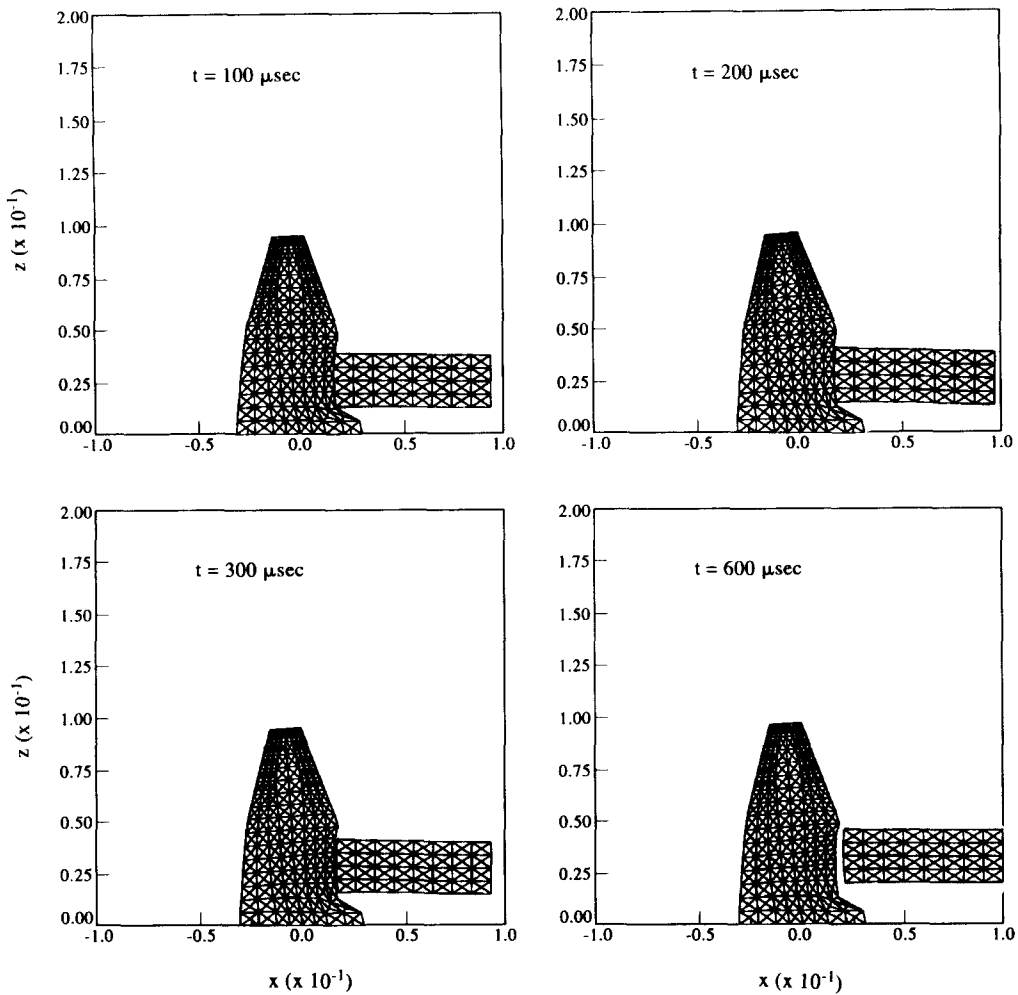


Fig. 7. Event 3. “Hard” low-impact EPIC92 hydrocode results.

The projectile also deforms permanently and $\bar{\epsilon}^p = 0.20$ is reached beneath the impact edge after 220 μs . With continued bending of the fuze, the plastic hinge widens somewhat, but then remains steady throughout the remainder of the impact process.

4.3. Event 3. “Hard” projectile, low-impact point

In contrast to the “hard” high-impact event, the “hard” low impact causes much less fuze bending, primarily because the low-impact occurs near the thick, rigidly-fixed fuze base where the bending stiffness is large (Fig. 7). Furthermore, because the impacted fuze surface is less oblique, the entire surface of the projectile contacts the fuze after 20 μs . This reduces both projectile rotation and slip along the fuze surface. The equivalent plastic strain contours are nearly symmetric about the contact region (Fig. 8b). In contrast to the high-impact event, the $\bar{\epsilon}^p = 0.20$ contours do not extend to the back side of the fuze, since there is not as much fuze bending. There is also a reduction in the contact time, and after 280 μs the projectile bounces off the fuze in elastic rebound. The impact simulation results are summarized in Table 1.

5. IMPACT EXPERIMENTS

In the experiment a 300 g cylindrical steel projectile is launched at 208 m/s from a 37 mm gun with a barrel diameter of 1.090 in. (27.7 mm). A schematic showing the relative positions of the fuze, projectile breakwire fixture for velocity measurement, X-ray tube and film plate,

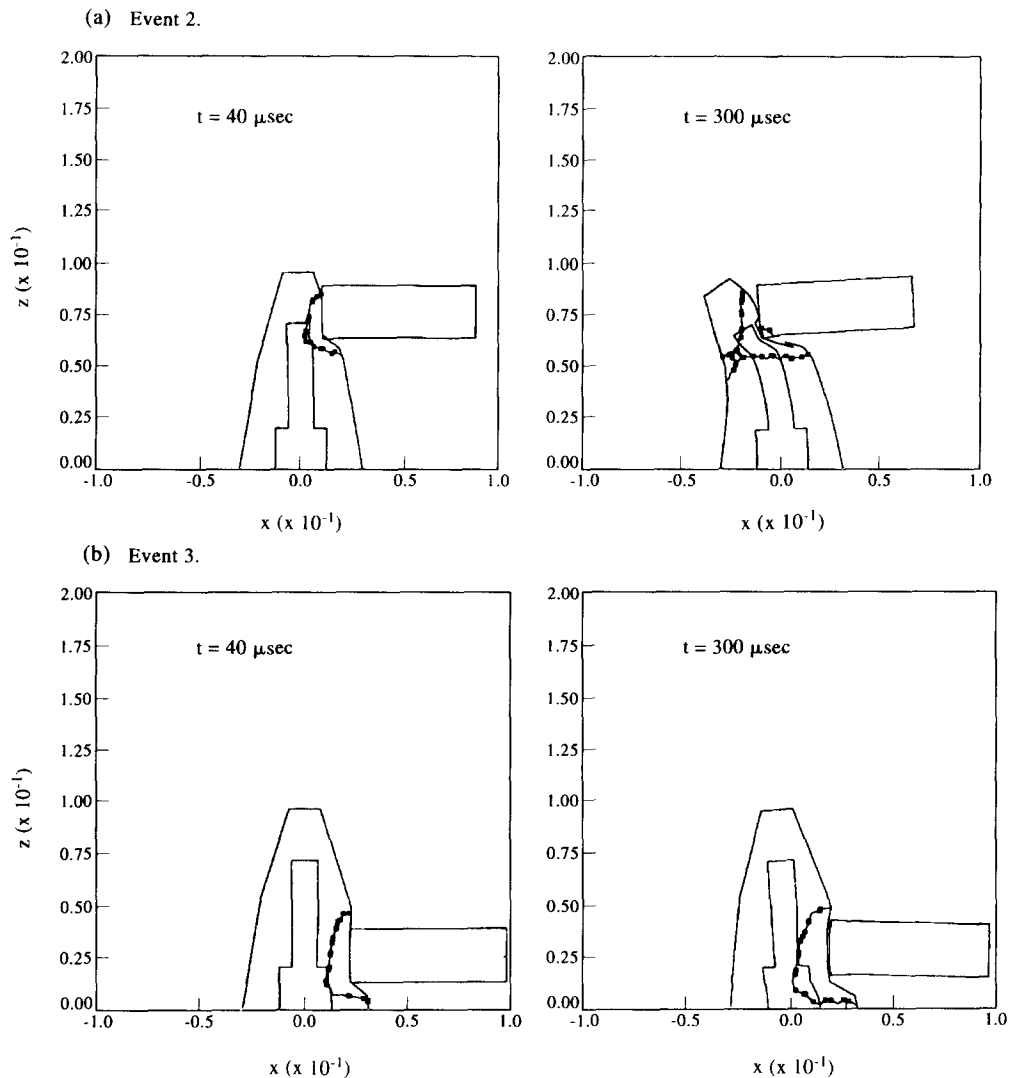


Fig. 8. $\varepsilon^P = 0.20$ contours for "hard" projectile impacts (a) Event 2. (b) Event 3.

Table 1. Summary of impact simulation results

	Shape of $\varepsilon^P = 0.20$ contours	Projectile rotation rate [†] (rev/s) & sense	Contact duration (μ s)	Tip angle of neutral fiber [†] (deg)	Tip displ. of neutral fiber [†] (nm)	Projectile deformation
Event 1		232.8				
"soft", high-impact	n/a	CW	420	37.3	30.7	moderate
Event 2	Asymmetric	-144.8				
"hard", high-impact		CCW	500	36.8	34.5	minimal
Event 3		0.8				
"hard", low-impact	symmetric	CW	280	3.7	7.9	minimal

[†]at 700 μ s.

and 16mm Hycam camera is given Fig. 9. The propelling charge consisted of 28 g of M2-165 mm gun propellant and was ignited using an M38 B-2 primer. An obturator was attached to the projectile during firing to reduce combustion gas emissions. Several pre-test shots verified the projectile velocity repeatability. The aim point was 1.25 in. (31.75 mm) below the fuze top but the actual impact point was 0.27 in. (6.8 mm) below the aim point.

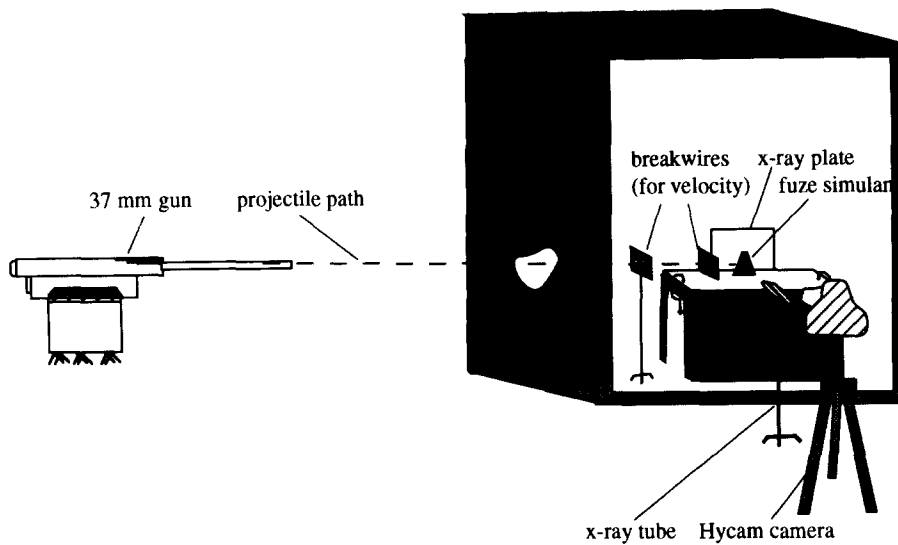


Fig. 9. Ballistic range configuration.

Based on the results of the simulation, it was desired to have a radiographic image of the impact event taken $250\text{ }\mu\text{s}$ after initial impact. The actual radiograph was taken $272\text{ }\mu\text{s}$ after impact, and we compared this radiograph with the hydrocode results at $280\text{ }\mu\text{s}$ (Fig. 10). At this instant, the brass core of the fuze is bent but not fractured, and the aluminum outerbody appears fractured through the cross-section. The projectile deforms by slightly bulging beneath the point of impact and the projectile's tail end is rotated slightly upward at this instant in the impact.

The steel projectile penetrated into the fuze to a maximum depth of approximately 13 mm and formed a circular indentation in the aluminum. The aluminum subsequently fractured and the fuze top was severed (Fig. 11). The fuze top fragment also contains a circular impact imprint in its surface. Also visible in Fig. 11 is the bolt that holds the fuze to the 0.25 in. (6.55 mm) thick rolled-homogeneous armor (RHA) base and the failed weld line in the RHA base plate. The weld in the RHA base plate failed during impact and the entire fuze assembly rotated backwards approximately 35° . This was an unanticipated fixture failure, and prevented quantitative comparisons between the experimental and numerical fuze deformation results. The projectile sustained little permanent deformation, although a small chip was visible on the edge beneath the impact point.

6. COMPARISON OF NUMERICAL AND EXPERIMENTAL RESULTS

The experimental results and the simulation results generally agree during the initial stages of the impact but depart significantly at later stages of the penetration. The reasons for the observed differences between the simulation and the experiment appear in the discussion below, and are related to (i) the inability of the hydrocode to effectively model fracture, and (ii) boundary condition differences between the experiment and those assumed in the numerical simulation.

The most obvious difference between our predictions and the experimental results is that in the experiment the fuze fails by fracture while we predict that the top of the fuze remains intact and connected to the fuze body for identical impact conditions. Despite the fact that the plastic "hinge" might suggest a failure location, the inability of the hydrocode to model gross, large-scale fracture in structures is a primary reason why there is a disparity between numerical impact results and the experiment. Instead, the hydrocode simulates fracture failure by eliminating an element's ability to sustain shear and tensile normal stress when the level of damage exceeds a critical level in that element. To address this type of fracture problem, the EPIC92 hydrocode would require an algorithm that permits finite element

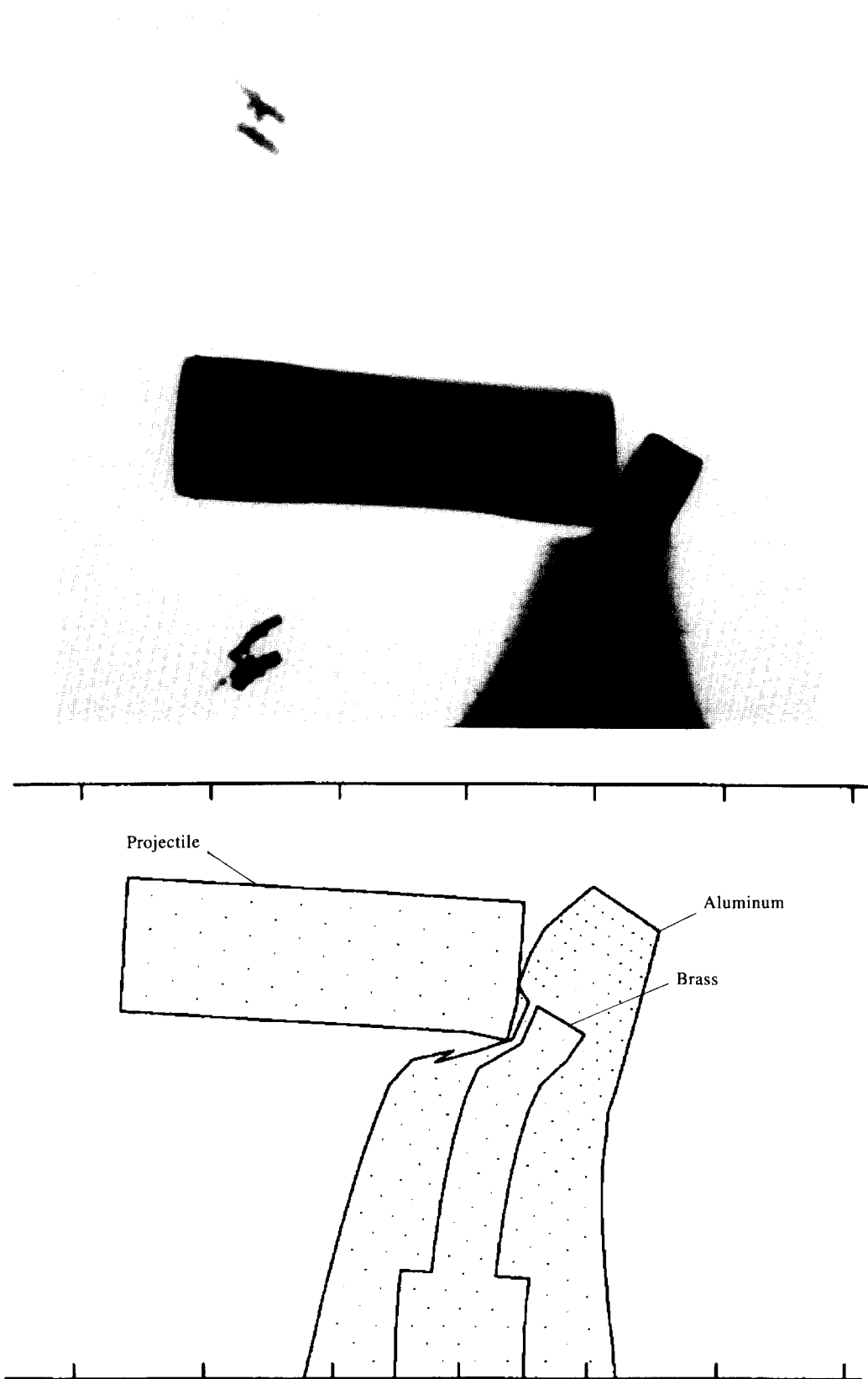


Fig. 10. X-ray radiograph of impact event at 272 μ s and EPIC92 hydrocode simulation at 280 μ s.

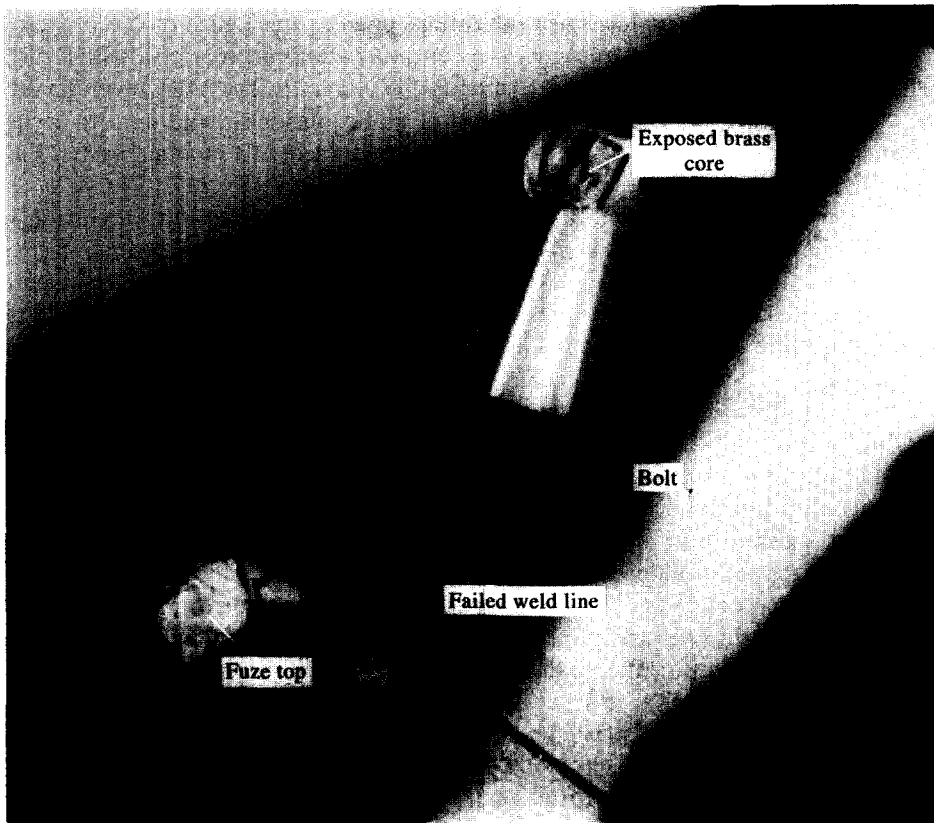


Fig. 11. Photograph of damaged fuze simulant showing severed fuze top with circular imprint of projectile.

mesh bifurcation when a critical energy release rate is attained or by using specialized crack-tip singularity finite elements [16].

The boundary conditions are somewhat different between the experiment and the numerical simulation, despite our efforts to minimize them. Boundary condition differences include, (i) modeling the contact surface as a frictionless interface, whereas in reality, contact friction can influence the deformation in low-speed impact problems, (ii) a disparity in the impact point and impact velocity between the experiment and the simulation. Additional hydrocode simulations could have been conducted to match the actual impact point in the experiment. However, the additional time and expense needed to conduct the additional simulations would not have added further insight into the render-safe problem, since the fundamental fracture physics could not be modeled by the hydrocode, and (iii) interface bonding differences between the brass core and the aluminum outerbody. Recall that in the experiment, the brass core was press-fitted into the aluminum outerbody and that given enough force, slip could occur along this interface. The interface was modeled so as to prevent slip in the numerical simulation. Furthermore, failure of the weld line in the experiment permitted the fuze body to rotate at its base, whereas the base of the fuze was rigidly fixed in the numerical simulation.

7. ANALYTICAL APPROACH

The fuze-projectile problem addressed earlier is reminiscent of a cantilever beam that is subjected to transverse impact. Although a complete review of the vast literature available on this topic is beyond the scope of this report, some notable works relevant to the current problem should be mentioned. Much of the original research on the transverse impact of

elastic–plastic beams was funded by organizations such as the Office of Naval Research and can be found, for example, in early issues of publications such as the *ASME Journal of Applied Mechanics*. Both Lee and Symonds [17] and Parkes [18] investigated the extent of applicability of using the methods of static plasticity solutions to dynamic problems. Their rigid–plastic analyses predict the development of a moving plastic “hinge”. Interestingly, a plastic hinge develops beneath the projectile in Event 2 (Fig. 8), a deformation feature which is common in problems addressed in the literature involving both quasistatic and impulsively-loaded elastic–plastic beams. For short beams, the effect of shear deformations are no longer negligible and their effects can be estimated by construction of so-called *interaction curves* using a plane stress approach [19, 20] or using a variational approach [21]. Hodge’s [21] analysis shows that for simply supported elastic–plastic short beams in which beam thickness is approximately equal to beam length (as in this work), the maximum load that the beam can sustain is reduced by approximately 20% if one includes the effects of shear in the analysis. Some of the discrepancies between theory and experiment discussed in Parkes’ [18] paper were re-examined by Ting [22, 23], whose analyses rigorously account for geometrical effects due to large plastic deformations of the rigid–plastic beam. Keer and Schonberg [24] solve an elastic cantilever beam problem subjected to two types of indentation displacement fields using a local elasticity solution coupled to a global beam theory solution approach. Both the local deformation effects of the indenter and the global deformation of the cantilever beam are modeled, however, the solution is limited to elastic media. Finally, Shu *et al.* [25] describe the mechanics of oblique impact of impulsively loaded cantilever beams in terms of axial and flexural components. Their model includes a mass of *finite* size at the beam tip, which produces a double “hinge” deformation mechanism. The model is used to explain why the observed curvature of the beam tip is less than that predicted by Parkes’ [18] single “hinge” model. Closed-form three-dimensional analytical solutions for transient loading of composite elastic–plastic bodies of variable cross-section do not appear in the literature so that a precise comparison with the hydrocode results is not possible. A closed-form solution to the elastic–plastic short beam impact problem would be invaluable to the explosive ordnance disposal community.

Often, the analytical solution to the “real” structural mechanics problem is intractable, whereas useful solutions can be obtained for a reduced or simplified version of the original problem. In this spirit, we consider the problem of an elastic–perfectly plastic cantilever beam, of circular cross-section, subjected to transverse impact as a model of the fuze impact problem. The analysis uses elementary beam theory with the following additional simplifying assumptions:

- small deformation theory
- beam inertia is neglected
- beam material is homogeneous (not composite) and elastic–perfectly plastic.
- shear stresses are neglected

The remainder of this Section is devoted to developing a simple analytical cantilever beam model of the fuze for estimating the total amount of strain energy absorbed by the fuze during impact. The analytical model results are then compared with the hydrocode predictions.

7.1. Deflections of a cantilever beam

The deflection curve of a beam can be shown to be governed by the following second-order ordinary differential equation [26],

$$\frac{d^2v}{dx^2} = -\frac{M}{EI} = \kappa, \quad (6)$$

in which v is the deflection, M is the bending moment applied to the beam, E is Young’s modulus, I is the cross-sectional moment of inertia about the neutral axis, and κ is the

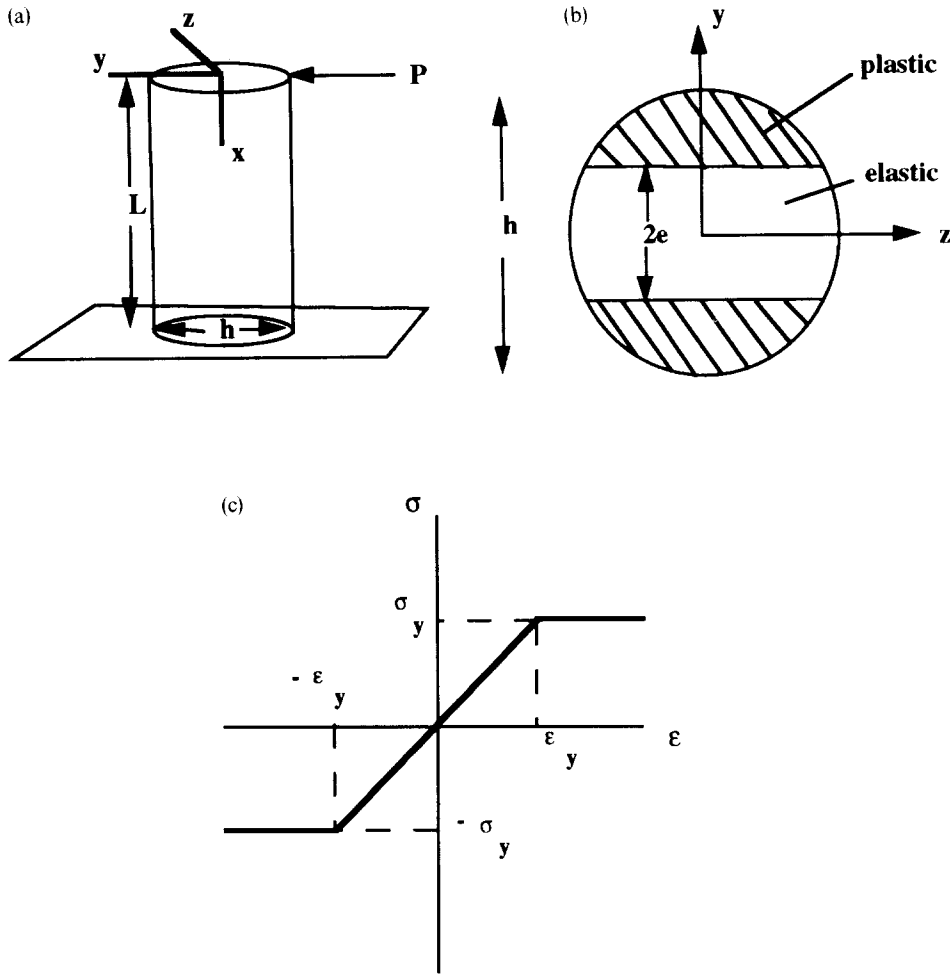


Fig. 12. Modeling simplifications. (a) Simplified fuze geometry (prismatic circular cantilever beam). (b) Beam cross-section showing integration coordinate system and regions of elastic and plastic behavior. (c) elastic-perfectly plastic material model.

curvature of the neutral axis. The quantity EI is known as the flexural rigidity of the beam. Two successive integrations of Eqn (6), with boundary conditions, $v(L) = v'(L) = 0$ (Fig. 12a), provide the solution, $v(x)$, for an end-loaded cantilever beam as,

$$v(x) = \frac{Px^3}{6EI} - \frac{PxL^2}{2EI} + \frac{PL^3}{3EI}, \quad (7)$$

in which L is the beam length, P is the magnitude of the end-load, and the bending moment is given by $M = -Px$. The maximum deflection occurs at the cantilever tip, $x = 0$, and is given by,

$$v_{\max} = \frac{PL^3}{3EI}. \quad (8)$$

7.2. Elastic-plastic deflections of a cantilever beam

Moment equilibrium of stress about the neutral axis of the beam yields the following integral expression for the resultant bending moment as,

$$M = \iint_A \sigma y \, dA, \quad (9)$$

in which σ is the longitudinal stress acting normal to an element of cross-sectional area, dA , and y is the distance from the neutral axis to dA . The fundamental assumption in slender beam theory is that plane sections remain plane, and normal to the longitudinal fibers of the beam so that the longitudinal strain, $\varepsilon = \kappa y$. For a beam made of an elastic (Hookean) material we have, $\sigma = E\varepsilon$, thus,

$$\sigma = \kappa E y. \quad (10)$$

It is clear from Eqn (10) that the maximum stress occurs at the outer fibers of the beam (Fig. 12b). For an elastic–perfectly plastic material the maximum stress is the yield stress (Fig. 12c) and we have,

$$\sigma_y = \kappa E e. \quad (11)$$

in which e is the distance from the neutral axis to the edge of the elastic core (Fig. 12b). Substitution of Eqns (10, 11) into Eqn (9) and using $(dA) = 2z(dy)$ in Eqn (9) for a beam of circular cross-section and diameter h , we arrive at,

$$M = \int_{-h/2}^{h/2} \sigma y dA = \frac{2\sigma_y}{e} \int_{-e}^e y^2 \sqrt{(h/2)^2 - y^2} dy + 4\sigma_y \int_e^{h/2} y \sqrt{(h/2)^2 - y^2} dy, \quad (12)$$

or,

$$M = \frac{3\sigma_y \sin^{-1}(2e/h)h^4 + \sqrt{h^2 - 4e^2}(10eh^2 - 16e^3)\sigma_y}{96e}. \quad (13)$$

The first integral on the right-hand-side of Eqn (12) represents the contribution to the bending moment due to elastic stresses while the second integral in Eqn (12) represents the contribution to the bending moment due to stress in the plastic region. Yielding begins to occur in the circular beam when $M = M_y$ or when,

$$\lim_{e \rightarrow h/2^+} M = M_y, \quad (14)$$

which gives for the *yield moment*, M_y , for the circular beam,

$$M_y = \frac{\sigma_y h^3 \pi}{32}. \quad (15)$$

As the bending moment of the beam increases, the region of purely elastic behavior shrinks until the maximum or limiting moment in the beam is reached. The limit is known as the *plastic moment*, M_p , and is obtained as,

$$\lim_{e \rightarrow 0^+} M = M_p. \quad (16)$$

For the beam of circular cross-section the plastic moment is given by,

$$M_p = \frac{\sigma_y h^3}{6}. \quad (17)$$

Timoshenko and Gere [26] define a *shape factor*, f , for a beam of given cross-sectional geometry as the ratio of the plastic moment to the yield moment, or $f = M_p/M_y$. For a beam of circular cross-section $f = 16/3\pi \cong 1.70$, as obtained by dividing Eqn (17) by Eqn (15). In the linear–elastic range, the relation between bending moment and curvature can be nondimensionalized [26] as follows,

$$\frac{M}{M_y} = \frac{\kappa}{\kappa_y} \quad 0 \leq M \leq M_y \quad (18)$$

Equation (18) is a linear function on a moment–curvature diagram (Fig. 13). However, as M increases beyond M_y , and the beam begins to yield, the moment–curvature relationship becomes nonlinear and the ordinate value approaches an asymptote representing the plastic moment, M_p , which is equivalent to the shape factor, f , as shown in Fig. 13. In the nonlinear range, the bending moment in Eqn (13) is nondimensionalized by dividing

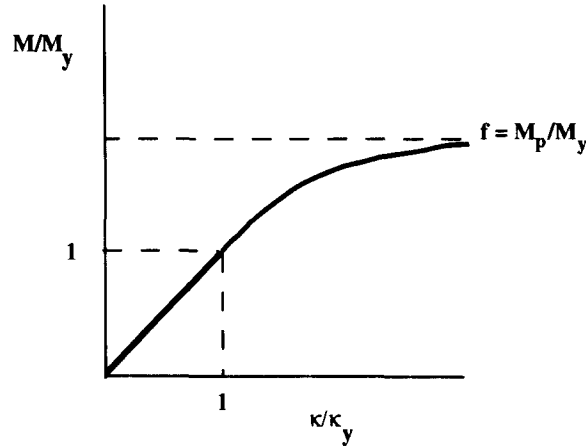


Fig. 13. Moment vs curvature relationship for an elastic-plastic cantilever beam.

by Eqn (15) to obtain,

$$\frac{M}{M_y} = \frac{3 \sin^{-1} \left(\frac{2\kappa_y}{\kappa} \right) \left(\frac{\kappa}{\kappa_y} \right)^4 + \sqrt{\left(\frac{\kappa}{\kappa_y} \right)^2 - 4} \left(10 \left(\frac{\kappa}{\kappa_y} \right)^2 - 16 \right)}{3\pi \left(\frac{\kappa}{\kappa_y} \right)^3}, \quad (19)$$

in which $\kappa/\kappa_y = h/2e$. By way of comparison, it can be shown that the moment–curvature relation for a rectangular beam takes on the relatively simple form [26],

$$\frac{M}{M_y} = \frac{3}{2} - \frac{\kappa_y^2}{2\kappa^2}, \quad M_y \leq M \leq M_p \quad (20)$$

which can be solved for the curvature ratio in terms of the moment ratio as follows,

$$\frac{\kappa}{\kappa_y} = \frac{\sqrt{2/2}}{\sqrt{\frac{3}{2} - \frac{M}{M_y}}}, \quad M_y \leq M \leq M_p. \quad (21)$$

The presence of the arcsine function in Eqn (19) makes the direct algebraic solution for κ/κ_y difficult. However, an approximate solution may be obtained by plotting Eqn (19) for given values of κ/κ_y and curve fitting the resulting nonlinear equation using a Marquardt–Levenberg (M–L) regression algorithm [27]. Equation (19) is plotted (Fig. 14) together with the following approximation obtained using the M–L method,

$$\frac{\kappa}{\kappa_y} \cong \frac{\sqrt{3/2}}{\sqrt{\frac{16}{3\pi} - \frac{M}{M_y}}}, \quad M_y \leq M \leq -M_p \quad (22)$$

where we have replaced the M–L derived numerical value, 0.86610, in the numerator of Eqn (22), with $\sqrt{3/2}$ to more closely resemble the form of the numerator in Eqn (21). Before we can determine the strain energy in the beam, we must determine the tip deflection, δ , as a function of the applied load, P . The tip deflection, δ , of the elastic–plastic beam may be determined by use of the *second curvature–area theorem* ([26], pp. 306–309) as follows,

$$\delta = \int_0^{x_1} \frac{Px^2}{EI} dx + \int_{x_1}^L \kappa x dx, \quad (23)$$

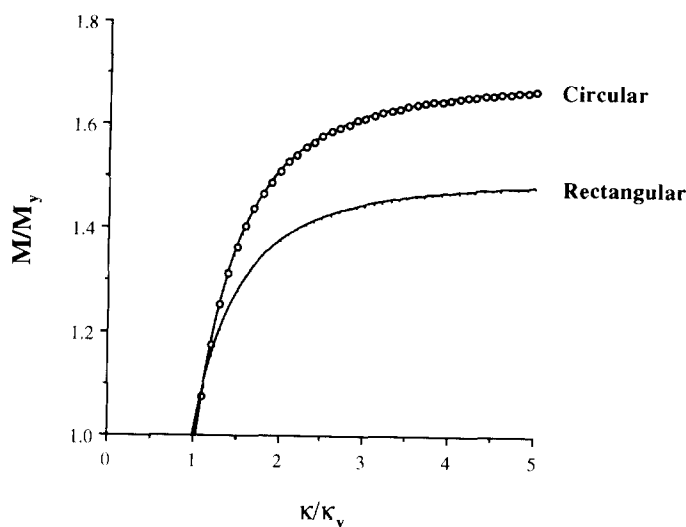


Fig. 14. Moment vs curvature plots for elastic-plastic cantilever beams of various cross-sections.

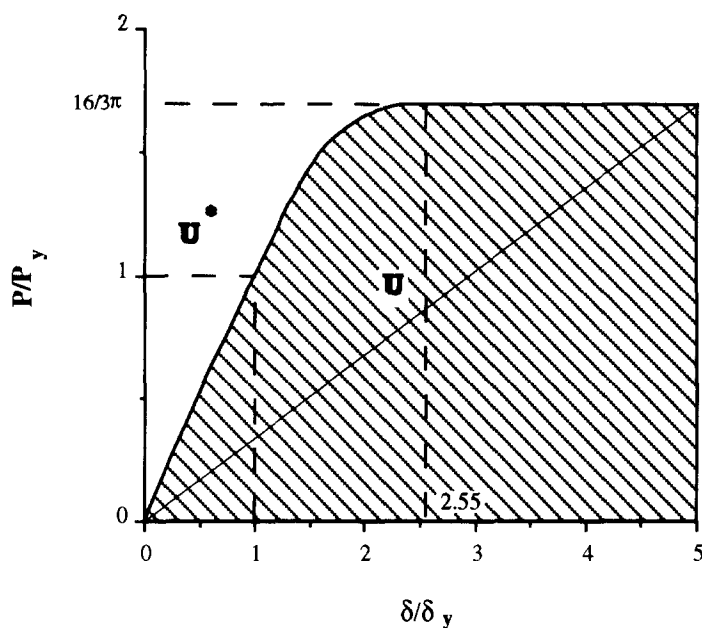


Fig. 15. Load vs deflection, Eqn. (24), for an elastic-plastic cantilever beam of circular cross-section.

in which x_1 represents the limit of purely elastic behavior in the beam. The tip deflection is evaluated by first substituting the approximate curvature expression, Eqn (22), into the integrand of the second integral in Eqn (23), and using the identities, $\kappa_y = M_y/EI$, $x_1 = M_y/P$, and $M_y = P_y L$. This results in the following approximate expression for the dimensionless deflection (plotted in Fig. 15),

$$\frac{\delta}{\delta_y} = \left(\frac{P_y}{P} \right)^2 \left[7.37 - 5.89 \left(1 + 0.294 \frac{P}{P_y} \right) \sqrt{\frac{16}{3\pi} - \frac{P}{P_y}} \right], \quad 1 \leq \frac{P}{P_y} \leq \frac{16}{3\pi} \quad (24)$$

in which $\delta_y = P_y L^3/3EI$, from Eqn (8), is the maximum elastic deflection at the yield load P_y . When $P/P_y = 16/3\pi$, the dimensionless deflection is $\delta/\delta_y = 2.55$.

7.3. Complementary energy of an elastic-plastic cantilever beam

The dimensionless complementary energy, U^* , in a beam subjected to inelastic bending may be obtained by integrating Eqn (24) with respect to P/P_y as,

$$U^* = \int_0^1 \frac{P}{P_y} d\left(\frac{P}{P_y}\right) + \int_1^{p_1} \frac{\delta(P/P_y)}{\delta_y} d\left(\frac{P}{P_y}\right). \quad (25)$$

The first term in Eqn (25) is the elastic contribution to the complementary energy while the second term is the elastic-plastic contribution to the complementary energy. Evaluation of these integrals gives the total dimensionless complementary energy of the beam,

$$U^* = \frac{1}{2} + (2\sqrt{3}(f - p_1)\sqrt{f - p_1} + (p_1 - 1) + \sqrt{3}\sqrt{f - 1}(3p_1 - 2f - 1))/p_1, \quad (26)$$

in which $p_1 = P/P_y$ and $f = 16/3\pi$. At the maximum bending load, $p_1 = f = 16/3\pi$, and $U^* = \frac{1}{2} + 1.005 = 1.505$ in Eqn (26). Also,

$$U^* + U = \frac{P}{P_y} \frac{\delta}{\delta_y}, \quad (27)$$

in which U is the dimensionless strain energy of the beam. Hence in Eqn (27), $U = (16/3\pi)(2.55) - 1.505 = 2.82$. This result shows that the total dimensionless strain energy, at the moment the plastic hinge is formed, is over 5.5 times the energy absorbed in the purely elastic bending regime, the ratio of plastic bending strain energy to total elastic bending strain energy is 0.96.

8. COMPARISON OF NUMERICAL AND ANALYTICAL RESULTS

In order to determine the strain energy in the elastic-plastic beam, we must first calculate realistic values of P_y and δ_y using the material properties of 6061-T6 aluminum. To simplify the analysis, the effect of the brass core material on the inelastic bending of the cantilever beam is not considered. We assume in our analysis that the cantilever beam is composed entirely of aluminum which is “stronger” than the brass up to an equivalent plastic strain of 0.20 (Fig. 3). Therefore, for a given deflection, our analysis would overestimate the beam bending strain energy for $\bar{\epsilon}^p \leq 0.20$, and underestimate the strain energy for $\bar{\epsilon}^p > 0.20$. However, a composite beam solution could be obtained by generalizing Eqn (12) to account for contributions to the moment equilibrium from both the brass and aluminum materials. The load at the onset of yield is a strong function of beam thickness, h , and is given by,

$$P_y = \frac{M_y}{L} = \frac{\sigma_y h^3 \pi}{32L}, \quad (28)$$

and the deflection at yield is,

$$\delta_y = \frac{\sigma_y h^3 \pi L^2}{96EI} = \frac{2\sigma_y L^2}{3Eh}, \quad (29)$$

in which the moment of inertia, $I = \pi h^4/64$. With $\sigma_y = 3.25$ kb (4.7×10^4 psi), $L = 2.47$ in. (62.7 mm) (measured from the impact point to the base), $E = 739$ kb (1.07×10^7 psi), $h = 2.4$ in. (61 mm), Eqns (28, 29) give, $P_y = 25,893$ lbf (115 kN), and $\delta_y = 0.0074$ in. (0.188 mm).

The effect of beam taper can be analyzed by recognizing that the fuze geometry consists of a nonprismatic (tapered) cone in which the diameter can be approximated with the expression, $h = h(x) = h_a + (h_b - h_a)x/L$. It can be easily shown by substitution of $h(x)$ into Eqn (28) that the load, P_y , required to cause yield is a function of position along the length of the cone of diameter, h_a , at the impact location, and of diameter, h_b , at the build-in end. Therefore Eqn (28) can be rewritten as,

$$P_y = \frac{\sigma_y \left(h_a + (h_b - h_a) \frac{x}{L} \right)^3 \pi}{32x}, \quad (30)$$

with similar substitutions required in the expressions for beam inertia, I , and deflection, δ_y . In a prismatic cantilever beam the position of maximum stress, σ_{\max} , and bending moment are coincident and occurs at the built-in end with diameter, h_b . However, in a tapered cantilever beam we find that the maximum stress is,

$$\sigma_{\max} = \frac{128PL}{27\pi h_a^2(h_b - h_a)}, \quad \text{at } x = \frac{h_a L}{2(h_b - h_a)}, \quad (31)$$

in which the position of σ_{\max} is determined by setting $d\sigma_y/dx = 0$ in Eqn (30). In the fuze problem, $h_b = 2.4$ in. (61 mm) and $h_a = 1.39$ in. (35.3 mm), so that σ_{\max} occurs at $x = 0.689L$ measured from the impact point toward the built-in end. In addition, we find that the ratio of maximum stress, σ_{\max} to the stress, σ_b , in the built-in end of the tapered beam to be,

$$\frac{\sigma_{\max}}{\sigma_b} = \frac{4h_b^3}{27h_a^2(h_b - h_a)}, \quad (32)$$

in which for the specific case of the fuze geometry we find that σ_{\max} is 5% greater at $x = 0.689L$ than σ_b at $x = L$ (σ_b is determined by letting $x = L$ in Eqn (30)). For the specific case of a tapered circular cantilever beam in which $h_b = 2h_a$, Timoshenko and Gere [26] find a 19% increase in σ_{\max} relative to σ_b which occurs at $x = 0.5L$. Our result in Eqn (32) is more general however, and reduces to the Timoshenko and Gere [26] result when $h_b = 2h_a$. The assumption that the fuze geometry is prismatic is not so bad since there is only a 5% difference between σ_{\max} and σ_b in a beam with the fuze geometry considered in this work.

An estimate of the average load, P , on the cantilever beam can be determined from the length of time it takes the projectile to decelerate and begin to rebound. Inspection of the fuze centerline nodal position vs time plot (Fig. 16) indicates that the projectile's velocity reversed at about $360 \mu\text{s}$ and that the amount of elastic rebound beneath the projectile is about 0.0298 in. (0.747 mm). The change in the projectile's momentum with respect to time is equal to the average impact force $P = 37,094$ lbf (165 kN) which is determined using an initial projectile velocity of 198 m/s and mass of 0.3 kg. The beam theory solution provided the value of $P_y = 25,893$ lbf (115 kN) from Eqn (28), so that $P/P_y = 1.43$. Since P_y is sensitive to the value chosen for h , see Eqn (28), if a slightly smaller value of h was used in the calculation, rather than the maximum value used of $h_b = h = 2.4$ in. (61 mm), P_y would dramatically decrease, and P/P_y would become $f = M_p/M_y = 16/3\pi = 1.7$. At this limit the beam is in a state of unrestricted plastic flow. A state of unrestricted plastic flow occurs in the fuze very

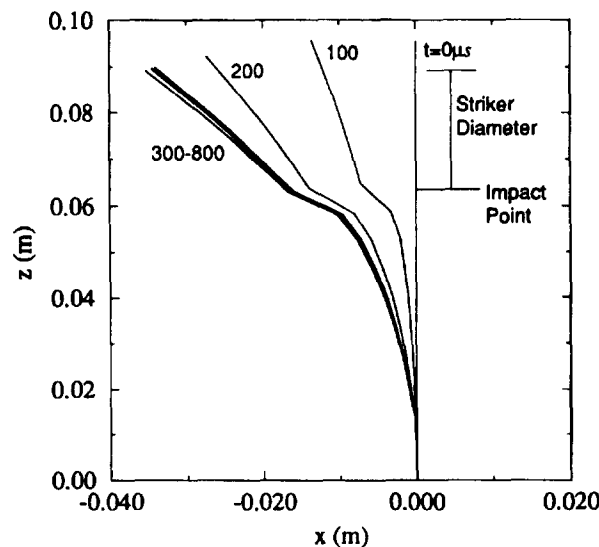


Fig. 16. Fuze centerline distortion (in meters) vs time for Event 2.

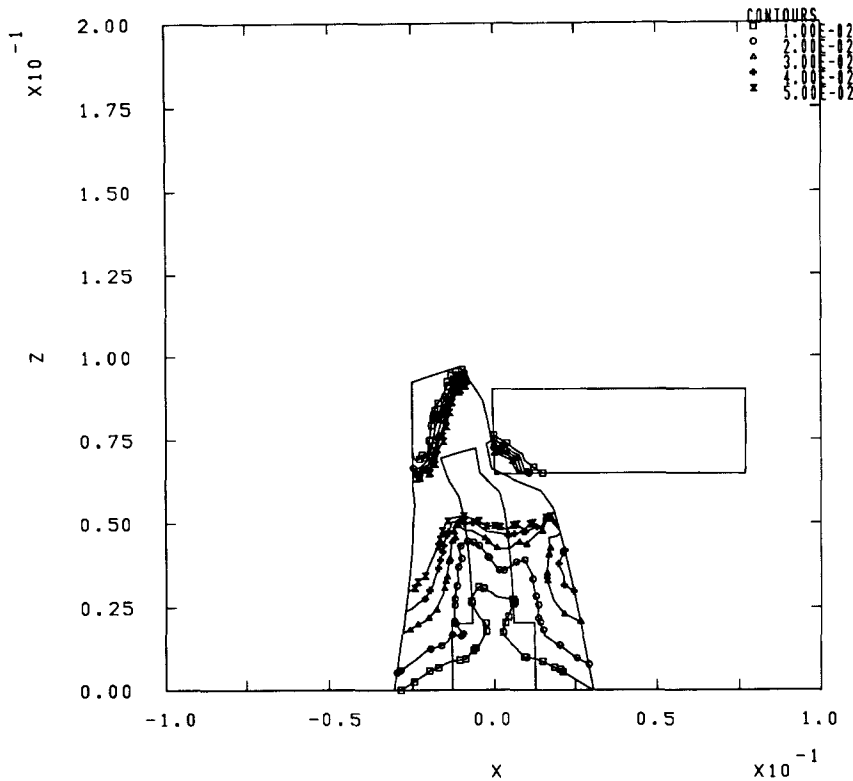


Fig. 17. Equivalent plastic strain contours at 120 μ s, showing fully developed plasticity across the diameter of the fuze.

early in the deformation history as seen in the well developed pattern of plastic strain through the fuze cross-section at 120 μ s (Fig. 17). The total strain energy absorbed by the fuze during impact can be estimated by assuming that $P/P_y = M_p/M_y = 16/3\pi = 1.7$ and $\delta_y = 0.0074$ in. (0.188 mm) from Eqn (29). The actual deflection beneath the load point from the numerical simulation at 360 μ s is $\delta = 0.657$ in. (16.7 mm), which results in $\delta/\delta_y = 89$. Hence, the total dimensionless strain energy absorbed by the fuze due to elastic-plastic bending is estimated with the aid of Fig. 15 to be,

$$U_{\text{Tot}} = \frac{P}{P_y} \left(\frac{\delta}{\delta_y} - 2.55 \right) + U = \frac{16}{3\pi} (89 - 2.55) + 2.8 = 149.5. \quad (33)$$

This energy is dimensionalized through multiplication by $P_y \delta_y$ which results in a total strain energy of 2387 ft. lbf or 3.24 kJ attributed to elastic-plastic bending of the fuze. The 0.3 kg projectile can impart 5.88 kJ of kinetic energy during impact. Therefore, the plastic bending energy is 55% of the initial projectile kinetic energy. The fuze also suffered a considerable amount of localized deformation beneath the projectile (Fig. 17). The energy absorbed by this localized deformation can be approximated by multiplying the average projectile indentation depth, δ_p , (estimated from the experiment) with the average impact force, P , resulting in $P\delta_p = (37,094) (0.45)$ in. lbf = 1.89 kJ. This localized plastic energy is 32% of the initial projectile kinetic energy. Hence, the energy absorbed in fuze bending is about 1.7 times greater than the energy dissipated by localized deformation beneath the projectile. In the Event 2 simulation, the EPIC92 code estimates that the total plastic work absorbed by the fuze is 91% of the initial projectile kinetic which is in close agreement to our analysis which predicts that 87% of the initial projectile kinetic energy is dissipated in plastic work. The EPIC92 code also predicts that the rotational kinetic energy associated with the rebounding projectile is only 1% of the initial projectile kinetic energy.

The analytical model of an elastic-plastic beam subjected to an end load provides insight, at least to the point of fracture, into the render-safe mechanics of fuzes. It is estimated that

55% of the initial projectile kinetic energy is dissipated in elastic–plastic fuze bending and 32% of the energy is dissipated in localized deformation beneath the projectile. These results are corroborated by the EPIC92 numerical results which predict that 91% of the projectile kinetic energy is dissipated into target plastic work; the remaining energy is primarily dissipated as plastic work in deforming the projectile.

9. CONCLUSIONS

1. The results of numerical hydrocode simulations of oblique impact of a cylindrical steel projectile onto an aluminum–brass composite fuze simulant indicate that projectile hardness is an important parameter that governs the deformation history of the fuze; a “soft” steel projectile impacted the fuze and created a gouge, elliptical in form, as it ricocheted off the fuze, whereas a “hard” steel projectile penetrated to a greater depth and bounced obliquely off the fuze.

2. Reasons for the observed disparity between the experiment and the hydrocode simulation of a materially and geometrically identical fuze impact problem include (i) the inability of the hydrocode to effectively model global fracture, and (ii) boundary condition differences between the experiment and the numerical simulation; in the experiment a weld line failed which provided an additional rotational degree of freedom, whereas in the numerical simulation the fuze maintains a rigid base. Nonetheless, the plastic “hinge” predicted in the simulation might suggest an indication of where the failure might be expected to occur.

3. The projectile’s sense of rotation during impact is related to projectile hardness and impact point as the numerical simulations indicate that the projectile (i) rotates clockwise in impact Event 1 involving the “soft” projectile, because of slip between the projectile and fuze, (ii) rotates counterclockwise in impact Event 2, involving the “hard” projectile, since the harder projectile penetrates into the fuze, thereby precluding slip, and (iii) remains relatively level in impact Event 3 as the obliquity of impact is less than in Events 1 and 2.

4. Positioning the gun close to the fuze during firing provides a lateral constraint to the projectile during impact. The practice would help prevent projectile rotation during flight and impact and would also reduce the variability in impact response that occurs as a result of projectile impact obliquity, impact location, and projectile hardness effects.

5. An analytical model of a cantilevered elastic–plastic beam subjected to an end load provides insight, at least to the point of fracture, into the render-safe mechanics of fuzes. For the case studied, it is estimated that 55% of the initial projectile kinetic energy is dissipated in elastic–plastic fuze bending and 32% of the energy is dissipated in localized deformation beneath the projectile. These results are corroborated by the EPIC92 numerical results which predict that 91% of the projectile kinetic energy is dissipated into target plastic work; the remaining energy is primarily dissipated as plastic work in deforming the projectile.

Acknowledgements—This work was supported by the Naval Explosive Ordnance Disposal (NAVEOD) Technology Center, Indian Head, Maryland under ARL work order number 4G015-414-R4. The authors would like to acknowledge the overall assistance of Mr Atul Patel of NAVFOD with regard to the fuze render-safe problem. Appreciation is also expressed to Mr Rich Gold of NAVFOD for expedient delivery of the projectile and fuze simulant used in the field test.

REFERENCES

1. A. Patel and R. Gold, Personal communication, U.S. Army Research Laboratory, Aberdeen Proving Ground, MD, October (1993).
2. J. M. McGlaun, F. J. Zeigler and S. L. Thompson, CTH: A three-dimensional, large deformation, shock wave physics code. SAND 87-0726C, Sandia National Laboratory, Albuquerque, NM (1987).
3. J. J. Monaghan, Why particle methods work. *SIAM J. Sci. Stat. Comput.* **3**, 422–433 (1982).
4. R. Tipton, CALE user’s manual, version 910701. Lawrence Livermore National Laboratory (1991).
5. G. R. Johnson, High velocity impact calculations in three dimensions. *J. Appl. Mech.* **99**, 95–100 (1977).
6. G. R. Johnson, R. A. Stryk, D. E. Pratt and J. A. Schonhardt, *EPIC Hydrocode User’s Workshop*. Alliant Techsystems, Inc., Brooklyn, Park, MN, October (1992).
7. G. R. Johnson, R. A. Stryk, D. E. Pratt and J. A. Schonhardt, *User Instructions for the 1992 Version of the EPIC Code*. Alliant Techsystems, Inc., Brooklyn, Park, MN, October (1992).
8. K. S. Holian, S. J. Mosso, D. A. Mandel and R. Henninger, MESA: A 3-D computer code for armor/anti-armor applications. LA-UR-91-569. Los Alamos National Laboratory Report. Los Alamos, NM (1991).

9. D. A. Matuska, HULL user's manual. Air force Armament Laboratory Report AD-A145000, Orlando Technology, Inc., Shalimar, FL, June (1984).
10. J. O. Hallquist and D. J. Benson, DYNA3D user's manual, UCID-19592, Rev. 2. Lawrence Livermore National Laboratory, Livermore, CA (1986).
11. S. B. Segletes, Mechanisms inducing jet rotation in shear-formed shaped-charge liners BRL-TR-3090, U.S. Army Ballistic Research Laboratory, Aberdeen Proving Ground, Maryland, March (1990).
12. H. D. Jones and F. J. Zerilli, Reaction kinetics of metallized explosives. *Proc. Materials Res. Soc. Symp., Structures and Properties of Energetic Materials*, Vol. 296, pp. 311–315 (1993).
13. O. C. Zienkiewicz, *The Finite Element Method Method*. McGraw-Hill, New York (1977).
14. E. Oberg, F. D. Jones and H. L. Horton, *Machinery's Handbook* (edited by H. H. Ryffel). Industrial Press, New York (1984).
15. G. R. Johnson and W. H. Cook, Fracture characteristics of three metals subjected to various strains, strain rates, temperatures and pressures. *Engng Fracture Mech.* **21**, 31–48 (1985).
16. A. R. Ingraffea, Theory of crack initiation and propagation in rock. In *Fracture Mechanics of Rock*, pp. 71–110 (edited by B. K. Atkinson) Academic Press, New York (1989).
17. E. H. Lee and P. S. Symonds, Large plastic deformations of beams under transverse impact. *J. Appl. Mech.* **19**, 308–314 (1952).
18. E. W. Parkes, The permanent deformation of a cantilever struck transversely at its tip. *Proc. Roy. Soc. Lond.* **A228**, 462–476 (1955).
19. A. P. Green, A theory of the plastic yielding due to bending of cantilevers and beams. Part II. *J. Mech. Phys. Solids* **8**, 148–155 (1954).
20. D. C. Drucker, The effect of shear on the plastic bending of beams. *J. Appl. Mech.* **23**, 509–514 (1956).
21. P. G. Hodge Jr., Interaction curves for shear and bending of plastic beams. *J. Appl. Mech.* **24**, 453–456 (1957).
22. T. C. T. Ting, The plastic deformation of a cantilever beam with strain-rate sensitivity under impulsive loading. *J. Appl. Mech.* **31**, 38–42 (1964).
23. T. C. T. Ting, Large deformation of a rigid, ideally plastic cantilever beam. *J. Appl. Mech.* **32**, 295–302 (1965).
24. L. M. Keer and W. P. Schonberg, Smooth indentation of an isotropic cantilever beam. *Int. J. Solids Struct.* **22**, 87–106 (1986).
25. D. Shu, W. J. Stronge and T. X. Yu, Oblique impact at the tip of a cantilever. *Int. J. Impact Engng* **12**, 37–42 (1992).
26. S. P. Timoshenko and J. M. Gere, *Mechanics of Materials*. Van Nostrand, New York (1972).
27. W. H. Press, B. P. Flannery, S. A. Teukolsky and W. T. Vetterling, *Numerical Recipes—The Art of Scientific Computing*. Cambridge University Press, New York (1986).